EES Catalysis

PAPER

View Article Online
View Journal | View Issue

Cite this: *EES Catal.*, 2023, 1, 562

Manipulating the spin state to activate the atomically dispersed Fe–N–C catalyst for oxygen reduction†

Fan Liu,[abc] Chengxiang Shi,[abc] Lun Pan,[abc] Zhen-Feng Huang,*[abc] Xiangwen Zhang[abc] and Ji-Jun Zou*[abcd]

Received 27th March 2023,
Accepted 21st April 2023

DOI: 10.1039/d3ey00066d

rsc.li/eescatalysis

Atomically dispersed metal–nitrogen carbon (M–N–C) catalysts with e_g^1 are believed to be very active for the oxygen reduction reaction; however, the activity origin of spin state manipulation is unclear. Here, using Fe–N–C as a model catalyst, we have developed a facile approach to manipulate its spin state from the low-spin to medium-spin state (Fe_{SAC}–NC, e_g^1) by utilizing the secondary coordination sphere effect of adjacent N=C–N moieties. The presence of N=C–N configurations with high electronegativity modifies the degree of hybridization between Fe $3d_{z^2}$, $3d_{xz}$ ($3d_{yz}$), and oxygen-containing intermediate π* orbitals, leading to an ideal balance between O_2 activation and *OH desorption. More impressively, we found that the catalysts with e_g = 1 in their metal centres may show very different activity, and the magnetic moment of $3d_{xz}$ + $3d_{yz}$ as a descriptor can accurately predict the ORR activity. Benefiting from the regulated coordination and electronic structures, the designed Fe_{SAC}–NC catalyst exhibited 3-fold mass activity and 7-fold specific activity than Pt/C.

Broader context

Fuel cells have been identified as prospective clean power contenders due to their high power density, environmental friendliness, and efficiency. Metal–nitrogen carbon catalysts with atomically dispersed Fe–N_x active sites have garnered a lot of attention as a possible non-noble metal-based catalyst class for the oxygen reduction process. A highly active Fe–N–C catalyst may be obtained *via* using an atomically dispersed metal framework that accurately controls the spin state of the active metal. However, given the different catalytic activities of catalysts with the identical spin state, it is highly difficult to adequately establish the structure–activity relationship between the catalytic activity and active site structure. In this study, we unveil the activity origin of atomically dispersed Fe–N–C catalyst by spin state manipulation and construct the targeted Fe–N–C catalysts with medium-spin state through utilizing the secondary coordination sphere effect of adjacent N=C–N moieties. Actually, the catalyst with e_g = 1 may show very different activity while magnetic moment of $3d_{xz}$ + $3d_{yz}$ is a more accurate descriptor to predict activity. This work fills in the gaps of e_g theory and unveils the ORR activity origin of M–N–C catalysts, providing new insights into precise customization of electronic structures of catalysts.

1. Introduction

The increasing energy crisis and environmental pollution caused by burning fossil fuels have motivated scientists to explore renewable energy conversions technologies such as fuel cells and metal–air batteries.[1–5] Oxygen reduction reactions (ORR), as the key reaction, involves multi-step proton and electron transfer and necessitate significant overpotential due to the sluggish reaction kinetics, which has become a major bottleneck.[6,7] Generally, noble metals such as Pt are the most active to accelerate ORR kinetics. Considering the scarcity, price, and low methanol crossover tolerance of noble metals, the development of stable and efficient non-precious metal catalysts is particularly important.[8,9]

M–N–C catalysts derived from low-cost and earth-abundant elements are very promising for ORR,[10,11] where the filling degree of d orbital in the metal center dominated by the oxidation state and spin state plays a central role in ORR. However, the active sites usually exhibit unsuitable spin states; for example, FeN_4 typically exhibits a low spin state, which has a relatively strong adsorption strength of oxygen-containing

[a] Key Laboratory for Green Chemical Technology of the Ministry of Education, School of Chemical Engineering and Technology, Tianjin University, Tianjin 300072, China. E-mail: jj_zou@tju.edu.cn, zfhuang@tju.edu.cn
[b] Collaborative Innovative Center of Chemical Science and Engineering (Tianjin), Tianjin 300072, China
[c] Zhejiang Institute of Tianjin University, Ningbo, Zhejiang, 315201, China
[d] Qinghai Quality Certification Consulting and Inspection Center Co., Ltd, Qinghai, China

† Electronic supplementary information (ESI) available. See DOI: https://doi.org/10.1039/d3ey00066d

intermediates, limiting the O_2 activation and *OH desorption.[12] Actually, the reduction of O_2 preferentially occurs on the Fe(III) site with a medium spin state, where one e_g electron ($t_{2g}^4e_g^1$) can readily penetrate the antibonding π-orbital of oxygen, resulting in relatively weak adsorption of oxygen-containing intermediates. Many efforts have been devoted to optimizing the spin-state of the Fe center, such as introducing a second metal,[13,14] doping electronegative non-metal elements (*e.g.* N, P, S, O),[15,16] and applying an external magnetic field.[17] These methods bring many complicated factors to the activity, however the investigation is solely focused on promoting O_2 activation or *OH desorption; thus, many important factors may be ignored. More significantly, the catalytic activity of medium spin (e_g^1) catalysts is not identical,[18,19] suggesting that the e_g theory does not apply in cases where there are several putative active sites with e_g^1 and thus cannot adequately describe the ORR activity origin. Thus far, it is challenging to thoroughly establish the structure–activity relationship between the catalytic activity and active site structure, particularly its spin state, let alone accurately fabricating specific spin state catalysts. Therefore, a better knowledge of the active origin of Fe–N–C catalysts is required to design better ORR catalysts.

Theoretically, the local charge distribution and spin state of the Fe active center can be modulated and its ORR intrinsic activity can be thus improved by manipulating the near-range coordinated atom species (primary coordination sphere) or long-range heteroatom interactions (secondary coordination sphere). Herein, we report an approach to manipulate the spin state of the Fe center by tuning the secondary coordination spheres in atomically dispersed Fe–N–C catalysts. ^{57}Mössbauer spectroscopy, X-ray absorption spectroscopy and density functional theory (DFT) calculations revealed that the insertion of neighbouring N=C–N configurations with high electronegativity can drive the spin state of Fe(III) transition from a thermodynamically stable low spin to a medium spin and modify the degree of hybridization between Fe $3d_{xz}$ ($3d_{yz}$) and oxygen-containing intermediates π* orbitals, which can optimize the adsorption energy for oxygen-containing intermediates, thereby leading to an ideal balance between O_2 activation and *OH desorption. More importantly, the catalysts with e_g^1 in their metal centers are found to exhibit significantly diverse activity, while the magnetic moment of $3d_{xz}$ + $3d_{yz}$ as a descriptor can precisely predict the ORR activity. Benefiting from the regulated coordination and electronic structures, Fe_{SAC}–NC exhibits excellent ORR catalytic performance and stability in alkaline electrolytes, surpassing conventional FeN_4 and commercial Pt/C catalysts. In a homemade zinc–air battery, the Fe_{SAC}–NC electrode delivered a higher maximum power density and discharge specific capacity than commercial Pt/C. This study fills in the gaps of the e_g theory and unveils the ORR activity origin of M–N–C catalysts, providing new insight into the precise customization of the electronic structures of catalysts.

2. Experimental

Synthesis of electro-catalyst

For the preparation of nitrogen-doped carbon, HBCT (20 mmol) and melamine (20 mmol) were dispersed separately in 50 mL of distilled water at 90 °C. Then, the two solutions were mixed and stirred for 20 min, followed by natural cooling to room temperature under stirring. The polymer was collected by filtration and dried, subsequently annealed at 400 °C for 2 h with a heating rate of 5 °C min^{-1} under a flowing N_2 atmosphere. The obtained nitrogen-doped carbon was denoted as NC. The as-synthesized NC material (500 mg) was dispersed in 200 mL of $FeCl_2{\cdot}4H_2O$ (0.5 mM) aqueous solution and stirred for 1 h. Then, the impregnated NC was separated by centrifugation and freeze-dried. After drying overnight, the dried material was annealed at 700 °C for 2 h with a heating rate of 5 °C min^{-1} under a flowing N_2 gas. Afterward, the sample was naturally cooled to room temperature and labelled as Fe_{SAC}–NC. At the same time, a typical FeN_4 catalyst was synthesized according to the literature for comparison.[20]

Characterizations

Scanning electron microscopy (SEM) observations were carried out on a Hitachi S-4800 microscope with an acceleration voltage of 530 KV. Transmission electron microscopy (TEM), high-resolution transmission electron microscopy (HR-TEM), and electron energy loss spectrum (EELS) observations were carried out on the Tecnai G2 F-20 microscope with an acceleration voltage of 200 KV. The high-angle annular dark field scanning transmission electron microscopy (HAADF-STEM) was carried out on a JEOL JEM-2100F with an acceleration voltage of 200 kV. X-ray photoelectron spectroscopy (XPS) analysis was conducted on a PHI-1600 X-ray photoelectron spectrometer using Al Kα radiation, and C 1s peak (284.8 eV) of contamination carbon was adopted to calibrate binding energy. The X-ray absorption fine structure spectroscopy (XAFS) measurement was carried out at Beijing Synchrotron Radiation Facility with a 1W2B beamline, using an incident beam monochromatized by Si (111) double crystal monochromators. X-ray diffraction (XRD) patterns were collected on a D8-Focus X-ray diffractometer system with Cu Kα radiation (λ = 1.5419 Å) with a scanning rate of 5° min^{-1}. Fourier transform infrared (FT-IR) spectrum was recorded on a Bruker FTIR spectrophotometer. Nitrogen physisorption experiments were conducted on a Micomeritics ASAP 2420 volumetric absorption analyzer at −196 °C.

Electrochemical measurements

All electrochemical measurements were carried out on the IVIUMSTAT workstation (Ivium Technologies BV, Netherlands) under the three-electrode system at room temperature. The catalyst was supported on a glassy carbon electrode (GCE) with a diameter of 5 mm (Pine Research Instrumentation Inc.) was used as a working electrode, whereas graphite rod and Ag/AgCl electrode were used as counter and reference electrodes, respectively. The cyclic voltammetry (CV) was carried out in O_2 or Ar-saturated 0.1 M KOH with a sweep rate of 50 mV s^{-1}. Linear sweep voltammetry (LSV) polarization curves were measured at 1600 rpm in O_2 saturated 0.1 M KOH electrolyte with a sweep rate of 10 mV s^{-1}. The rotating ring disk electrode (RRDE) analysis was also run in Ar or O_2 saturated 0.1 M KOH electrolyte with a rotation speed of 1600 rpm and the applied ring voltage was 1.125 V *vs.* RHE. LSVs rotated between

400 and 2025 rpm were obtained under an uninterrupted O_2 flow, in which the sweep window and rate were 0.2 to 1.2 V *vs.* RHE and 10 mV s^{-1}, respectively. Catalyst inks were prepared by dispersing 2.5 mg of the catalyst and 0.5 mg carbon in 980 μL of a mixed solvent (water and isopropanol in a 3 : 1 volume ratio) and 20 μL of a 5 wt% Nafion solution, with 30 min of sonication to obtain a uniform suspension. Then, 10 μL of homogeneous ink was dropped on a glassy carbon electrode (area, 0.196 cm^2) and fully dried in air at room temperature. The mass loading of the electrocatalyst on glassy carbon was 0.128 mg cm^{-2}.

DFT calculations

All DFT calculations were performed using the Vienna *ab initio* simulation package (VASP).[21] The generalized gradient approximation (GGA) and Perdew–Burker–Ernzerhof (PBE) functional were used to address the nonlocal exchange-correlation energy. The DFT+*U* method with $U = 4.0$ eV was applied to eliminate Fe 3d orbital self-interaction error. The cutoff energy and Brillouin zone integration were set to 520 eV and 2 × 2 × 1, respectively. The force and energy convergence criteria of structure optimization were 0.03 eV $Å^{-1}$ and 1×10^{-5} eV. All electronic structure calculations were performed using a 6 × 6 × 1 *k*-point grid. Spin polarization was considered in our calculations. To eliminate spurious periodic interactions, a 15 Å vacuum slab was added in the *z*-direction.

3. Results and discussion

3.1 Synthesis and characterization of Fe_{SAC}–NC

Fe_{SAC}–NC was synthesized *via* a combined hydrothermal and pyrolysis strategy, as illustrated in Fig. 1(a). First, 1,3,5-benzenetricarboxylic acid (HBCT) and melamine were mixed at 90 °C to enable self-assembly. As shown in FT-IR spectroscopy (Fig. 1(b)), the decrease in the intensity of the peaks associated with amine and carboxy groups of the obtained polymer revealed the amidation reaction between melamine and HBCT. Subsequently, porous nitrogen-doped carbon (NC) was obtained by pyrolyzing the polymer at 400 °C. Next, NC and $FeCl_2{\cdot}4H_2O$ were dispersed in a solvent and freeze-dried, ensuring the impregnation of ferric salt on NC. Finally, Fe_{SAC}–NC was obtained by pyrolyzing impregnated NC at 700 °C under an N_2 atmosphere. The nitrile group (–CN) at 2235 cm^{-1} of NC was not detected in Fe_{SAC}–NC, suggesting that the –CN group underwent a transformation and became involved in the creation of FeN_x active sites. The FeN_4 catalyst was synthesized as a reference using the same synthetic strategy.[20]

From scanning electron microscopy (SEM) images (Fig. S1, ESI†), the NC presents a bark-like structure on the surface. After adsorbing Fe and pyrolysis in the N_2 atmosphere, Fe_{SAC}–NC displays a flower-like nanostructure with a large number of mesopores. Bright-field transmission electron microscopy (TEM) images in Fig. 1(c) and (d) display amorphous carbon substrate without visible Fe nanoparticles in Fe_{SAC}–NC. Electron energy loss spectrometer (EELS) elemental analyses (Fig. S2, ESI†) confirmed the loading of Fe element in the porous carbon skeleton.

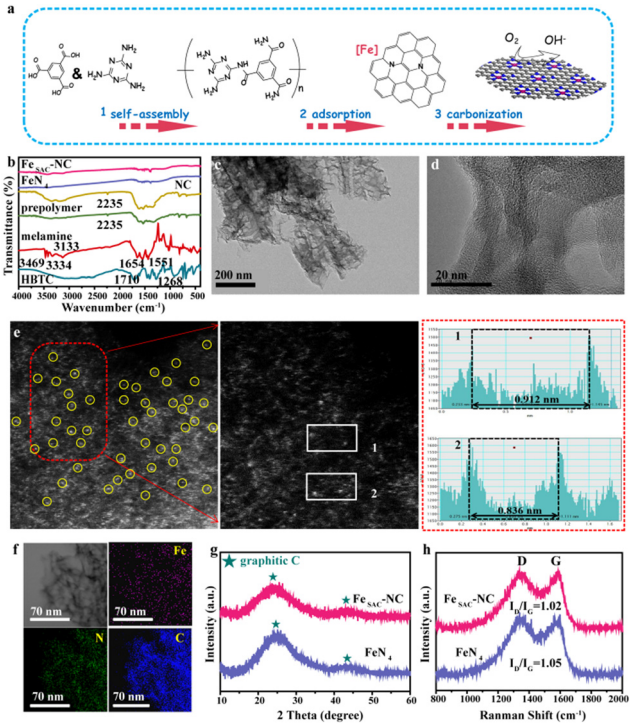

Fig. 1 (a) Schematic representation of preparation for Fe_{SAC}–NC. (b) FT-IR spectra of HTBC, melamine, prepolymer, NC, FeN_4, and Fe_{SAC}–NC. (c) and (d) TEM and HRTEM images of Fe_{SAC}–NC. (e) Aberration-corrected HAADF-STEM image of Fe_{SAC}–NC (left). Middle: The enlarged image of Fe_{SAC}–NC as marked by the red box. Right: Intensity distributions between two Fe atoms. (f) EDS element mapping of Fe_{SAC}–NC. (g) XRD pattern of Fe_{SAC}–NC and FeN_4. (h) Raman spectra of Fe_{SAC}–NC and FeN_4.

The aberration-corrected high-angle annular dark field-scanning transmission electron microscopy (HAADF-STEM) was performed to observe their structures in detail, and the results obtained are shown in Fig. 1(e). Due to the contrast difference of Fe with N and C, single Fe atoms are directly observed in the form of isolated brighter spots and homogeneously dispersed on the entire carbonaceous support. Furthermore, the space between two Fe atoms was 0.8 nm (Fig. 1(e), right) far exceeding the Fe–Fe bond length (0.248 nm), which consolidated the isolated atom feature of Fe in Fe_{SAC}–NC. EDS elemental mapping images (Fig. 1(f)), further manifest the uniform dispersion of C, N, and Fe elements in Fe_{SAC}–NC. X-ray diffraction (XRD) was employed to investigate the crystalline structure. As illustrated in Fig. 1(g), two broad peaks at approximately 25.0° and 44.0° correspond to (002) and (101) phases of carbon, respectively (JCPDS no. 41-1487).[22] Both Fe_{SAC}–NC and FeN_4 showed negligible Fe or FeO_x signals, indicating that the Fe atoms are in atomic separation. As viewed in Fig. 1(h), the I_D/I_G value of Fe_{SAC}–NC is 1.02, with a graphitization degree similar to FeN_4 (I_D/I_G = 1.05). The BET surface area of Fe_{SAC}–NC is 725 m^2 g^{-1}, much higher than that of NC (255 m^2 g^{-1}), suggesting increased surface area by creating mesopores. However, compared with FeN_4, which features a high surface area (752 m^2 g^{-1}), Fe_{SAC}–NC possessed a slightly lower surface area (Table S1, ESI†). The isotherm curves of

Fe_{SAC}–NC present a typical IV profile with a classical H4-type hysteresis loop,[23,24] revealing the well-developed micropores and the mesoporous structure (Fig. S3 and S4, ESI†). The formation of a mesopore-dominated porous structure in Fe_{SAC}–NC is attributed to the thermal decomposition of NC in the second heat treatment. The mesopore-dominated structure can boost the ORR performance by providing more nanochannels for fast reactant transportation and more active sites, which can readily adsorb and react with the reactants. The metal content in Fe_{SAC}–NC was analyzed using inductively coupled plasma atomic emission spectrometry (ICP), as shown in Table S2 (ESI†). The ICP combined with the elemental analyzer indicates the coexistence of C (81.38 wt%), N (8.97 wt%), O (3.21 wt%), Fe (5.79 wt%), and H (0.96 wt%) in Fe_{SAC}–NC. The Fe content measured from ICP is similar to that obtained from TGA analysis (Fig. S5, ESI†). Notably, the N/Fe atomic ratio of Fe_{SAC}–NC is approximately 6 : 1, significantly higher than that of FeN_4 (4 : 1), which means abundant N species are embedded in the structure.

X-ray absorption spectroscopy (XAS) measurements including X-ray absorption near-edge structure (XANES) and extended X-ray absorption fine structure (EXAFS) spectra were conducted to detect the electronic and coordination structure, with Fe foil, Fe_2O_3, iron(II) phthalocyanine (FePc), and FeN_4 as references. The formation of single atom Fe species was confirmed from Fe K-edge EXAFS spectra, where both Fe_{SAC}–NC and FeN_4 present a primary peak corresponding to the Fe–N scattering path (Fig. 2(a)). However, the major Fe–N peak in Fe_{SAC}–NC situated at 1.47 Å is larger than that in FeN_4 (1.44 Å). The quantitative EXAFS fitting result shows that the Fe atom in Fe_{SAC}–NC is coordinated with four-N atoms, forming a Fe–N_4 moiety in the first shell (Fig. S6 and Table S3, ESI†). In the pre-edge region, a peak specified as a 1s–3d transition at 7113 eV is detected in FePc and FeN_4, which is regarded as the fingerprint of the square-planner Fe–N_4 configuration. A decreased pre-edge peak intensity of Fe_{SAC}–NC implies the emergence of a broken square-planar structure with D_{4h} symmetry owing to the Fe–C scattering path.[25] The normalized XANES spectra show that the near-edge absorption of the Fe K-edge of Fe_{SAC}–NC is between FePc and Fe_2O_3, indicating that the average oxidation state of Fe is between +2 and +3 (Fig. 2(b) and Table S4, ESI†). Meanwhile, the absorption edge position for FeN_4 is similar to that of FePc, elucidating that the oxidation state of Fe is approximately +2. This suggests that the oxidation state of Fe in Fe_{SAC}–NC is higher than that in FeN_4.

The N K-edge XANES spectra were collected to probe the N coordination structure. As shown in Fig. 2(c), three peaks were observed for FeN_4, denoted as N1 to N3. The peak N1 at 399.8 eV is attributed to the N 1s → π* transition in aromatic N atoms of heterocyclic rings, π*(C═N–C). The peak N2 at 401.7 eV is assigned to the graphitic threefold N atoms

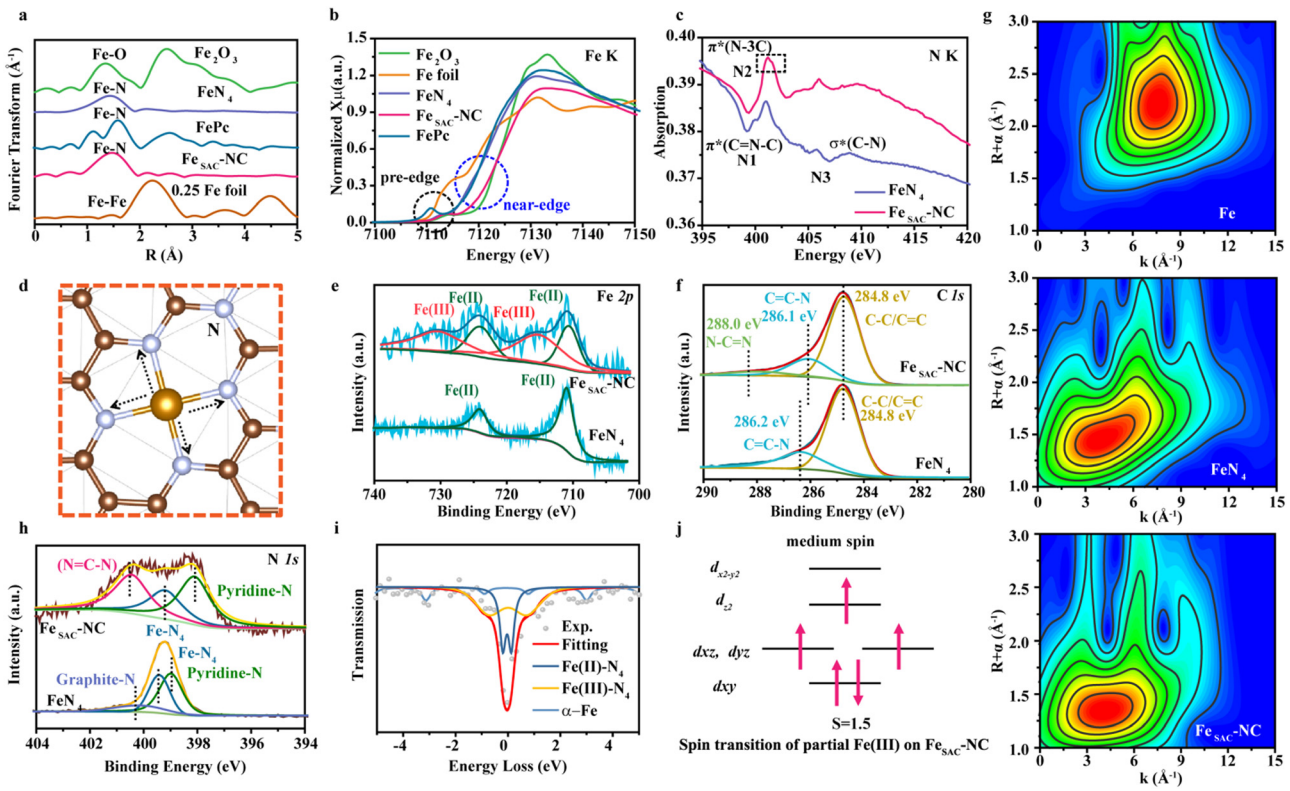

Fig. 2 (a) The k^2-weighted Fourier transform EXAFS spectra of Fe_{SAC}–NC, Fe_2O_3, Fe foil, FePc, and FeN_4. (b) The normalized XANES spectra at the Fe K-edge. (c) The normalized XANES spectra at the N K-edge. (d) The model of Fe_{SAC}–NC (gold: iron, silvery: nitrogen, brown: carbon). (e) XPS spectra of Fe 2p. (f) XPS spectra of C 1s. (g) Wavelet transform plots of Fe foil, FeN_4, and Fe_{SAC}–NC. (h) XPS spectra of N 1s. (i) Room-temperature ^{57}Fe Mössbauer spectrum of Fe_{SAC}–NC. (j) Schematic representation of the spin transition of Fe(III).

π*(N–3C). The peak N3 could not be assigned to any N species, derived from the general transition from the N 1s core level to C–N σ* states.[26] It is worth noting that the peak N2 splits into double peaks for Fe_{SAC}–NC, confirming that a portion of graphitic N is bonded to extra N atoms and forms N═C–N coordination-like DNA at 401.4 eV,[27,28] rather than direct coordination with metal Fe in the first shell, which is substantially different from FeN_4. Fig. 2(d) shows a detailed schematic of the N═C–N configuration in Fe_{SAC}–NC. The bonding between C═N and N atoms, thereafter initiates a slight asymmetrical expansion of the original Fe–N bonds (FeN_4: 1.89 Å and Fe_{SAC}–NC: 1.90 Å), which is consistent with the EXAFS spectra (Fig. 2(a) and (d)). The normalized C K-edge XANES spectra of FeN_4 and Fe_{SAC}–NC are shown in Fig. S7 (ESI†). The slight positive shift of the binding energy and the decrease in the peak intensity on π* (C–N) in Fe_{SAC}–NC confirm the existence of the N═C–N configuration because C exhibits lower electronegativity compared to N. As shown in Fig. 2(g), Fe_{SAC}–NC, and FeN_4 show WT-maximum with the k values of 4.1 $Å^{-1}$ and 4.0 $Å^{-1}$ for the Fe–N path, respectively, which is clearly distinguished from the Fe–Fe path (k = 7.5 $Å^{-1}$). Note that the deviation of the Fe–N path results presumably from the N═C–N configuration for Fe_{SAC}–NC.

X-ray photoelectron spectroscopy (XPS) characterization was carried out to probe the composition and chemical structure. As shown in Fig. 2(e), FeN_4 shows only two Fe 2p XPS peaks at 711.0 and 724.2 eV derived from Fe(II)–N_4.[29] In contrast, Fe_{SAC}–NC possesses a larger proportion of Fe(III)–N_4 (714.5 and 732.2 eV), consistent with the higher oxidation state.[30] The Fe(III)–N_4/Fe(II)–N_4 area ratio is 2 : 1, implying that Fe is mainly in the form of Fe^{3+} for Fe_{SAC}–NC. Fig. 2(f) displays the C 1s peaks at 284.8 eV, 286.1, and 288.0 eV for Fe_{SAC}–NC, which can be assigned to C–C═C, C–N, and N–C═N species,[31,32] respectively, consistent with the C and N K-edge XANES spectra. Fig. 2(h) displays the N 1s peaks at 398.1, 399.2, and 400.5 eV for Fe_{SAC}–NC, which can be assigned to pyridine-N, Fe–N_4, N–C═N (graphite-N), respectively.[20,33] Compared with FeN_4, the position of pyridine-N and Fe–N_4 of Fe_{SAC}–NC are shifted towards lower energy, implying that the electrons transfer from Fe to N (Fig. 2(h)). The considerable increase in the graphite-N content in Fe_{SAC}–NC over FeN_4 further demonstrates that the presence of N–C═N configuration.

^{57}Mössbauer spectroscopy was further used to quantify the spin state of atomic Fe–N_x sites. The first two doublets were the characteristics of Fe–N–C catalysts (FeN_4) ascribed to a ferrous low-spin Fe(II)–N_4 (D1) and a ferrous mediate-spin Fe(II)–N_4 (D2).[34,35] Previous research identified the D1-related component as the ORR active site in Fe–N–C catalysts.[36] Notably, Fe_{SAC}–NC contains three components: D1, D3, and sextet1, which are assigned to Fe(II)–N_4, Fe(III)–N_4, and α-Fe (Fig. 2(i) and Table S5, ESI†).[37,38] According to the values of quadrupole splitting (QS), the doublets D1 and D3 have been assigned to, mainly, low-spin Fe(II)–N_4 species (S = 0) and medium-spin Fe(III)–N_4 species (S = 3/2), respectively. Compared to the case of FeN_4, it can be seen that the incorporation of the N═C–N configuration induces a new medium spin Fe(III). The medium spin Fe^{3+} has an electron configuration of $d_{xy^2}d_{yz^1}d_{xz^1}d_{z^21}$ and shows lower e_g filling with favorable adsorption strength of oxygen-containing intermediates (Fig. 2(j)), and is thus more active for ORR.[37] Furthermore, the area of D1 and D3 is 30.2% and 61.7%, respectively, indicating that Fe_{SAC}–NC is mainly composed of medium spin Fe(III)–N_4 species.

On the basis of the above analysis, we can conclude that the coordination structure of Fe_{SAC}–NC involves a Fe central atom surrounded by four nitrogen atoms in the first shell, with an N═C–N configuration in the second shell. Such a coordination structure can readily trigger the electron transfer from Fe atoms to N and then to N═C due to the relatively high electron affinity of N.

3.2 ORR electrocatalytic performance of F_{eSAC}–NC

Fig. S8 (ESI†) shows the cyclic voltammetry (CV) curves of Fe_{SAC}–NC in O_2 and Ar-saturated solution. In contrast to the virtually featureless CV curves measured in the Ar-saturated solution, a notable cathodic peak appears in the O_2-saturated solution, which can be attributed to the reduction of O_2. The ORR peak of Pt/C appears at 0.84 V, while the ORR peak of Fe_{SAC}–NC reaches 0.89 V, approximately 50 mV higher than that of Pt/C, suggesting that Fe_{SAC}–NC shows higher ORR activity than commercial Pt/C.

The linear scanning voltammetry (LSV) was adopted to further investigate the ORR activity, as shown in Fig. 3(a). NC delivers an extremely low activity (Fig. S9, ESI†). In Fig. 3(a) and

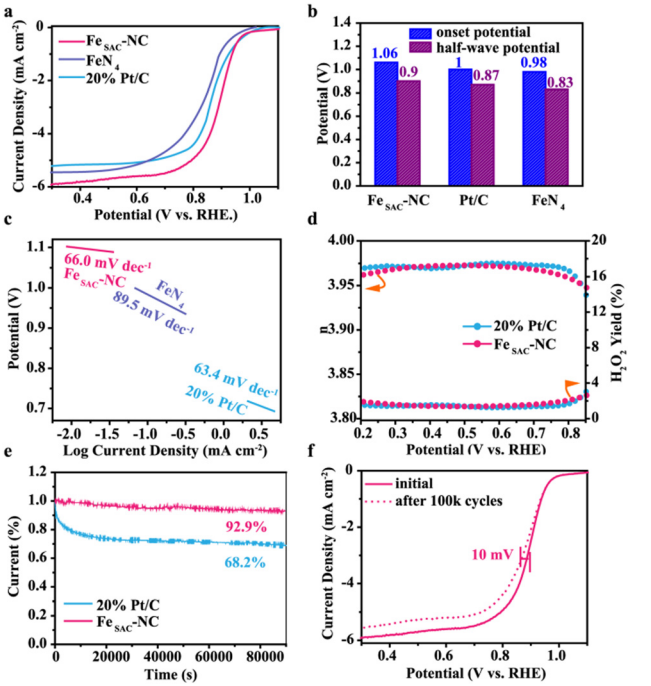

Fig. 3 (a) The LSV curves of Fe_{SAC}–NC, FeN_4, and 20% Pt/C in 0.1 M KOH. (b) The onset potential and half-wave potential of Fe_{SAC}–NC, FeN_4, and 20% Pt/C. (c) Tafel plots of Fe_{SAC}–NC, FeN_4, and 20% Pt/C. (d) Electron transfer number (n) and H_2O_2 yield calculated from RRDE measurement of Fe_{SAC}–NC and 20% Pt/C. (e) Stability evaluation of Fe_{SAC}–NC and 20% Pt/C. (f) LSV curves of Fe_{SAC}–NC before and after 100k cyclic voltammetry cycles.

(b), Fe_{SAC}–NC displays excellent activity with an onset potential of 1.06 V and a half-wave potential ($E_{1/2}$) of 0.90 V and even exceeds commercial Pt/C. Remarkably, compared with FeN_4, Fe_{SAC}–NC exhibits enhanced electrocatalytic performance toward ORR, indicating that the formation of medium spin Fe^{3+} further improves the ORR activity. As for the reaction kinetics, Fe_{SAC}–NC possesses an ultrahigh kinetic current density (J_k) of 44.4 mA cm^{-2} at 0.80 V, nearly an order of magnitude higher than that of commercial Pt/C (J_k, 7.89 mA cm^{-2}). The superior ORR kinetics of Fe_{SAC}–NC was further confirmed by the Tafel slope. The Tafel slopes of Fe_{SAC}–NC, 20% Pt/C, and FeN_4 were 66.0, 63.4, and 89.5 mV dec^{-1}, respectively, implying that Fe_{SAC}–NC possessed more favorable ORR kinetics compared with FeN_4 (Fig. 3(c)). The corresponding turnover frequency (TOF) of Fe_{SAC}–NC was 44.06 s^{-1}, outperforming that of Pt/C (4.81 s^{-1}),[39] suggesting that the Fe_{SAC}–NC possessed outstanding intrinsic ORR activity. The mass activity and specific activity of Fe_{SAC}–NC are 0.64 mA μg_{Fe}^{-1} and 2.10 mA cm_{Fe}^{-1}, respectively, three times and seven times higher than that of Pt/C (0.2 mA μg_{Pt}^{-1} and 0.31 mA cm_{Pt}^{-1}). Additionally, the ORR activity of Fe_{SAC}–NC in this work surpasses that reported for most near-term reported single atoms-based electrocatalysts (Table S6, ESI†).

Fig. S10a (ESI†) shows the LSV curves of Fe_{SAC}–NC measured at different rotating speeds. The current density goes up rapidly with the increase in the rotating speed. Fig. S10b (ESI†) exhibits Koutecky–Levich (K–L) plots of Fe_{SAC}–NC at different polarizing potentials, which show excellent linearity under different potentials, suggesting that the transferred electron numbers per O_2 molecule in the ORR process are almost the same. The average electron transfer number (n) of ORR for Fe_{SAC}–NC is 3.97 approaching that of Pt/C (n = 3.98), which manifests an efficient four-electron transfer process on Fe_{SAC}–NC. As shown in Fig. S11 and S12 (ESI†), the calculated average electron transfer number for FeN_4 is 3.89 because the Fe centers catalyze the formation of undesirable H_2O_2 products.[30,40] Therefore, medium spin Fe^{3+} in Fe_{SAC}–NC can avoid the possible Fenton reaction. To quantitatively evaluate the intermediate peroxide product, the RRDE measurement was performed. As shown in Fig. 3(d), the measurement conducted on the RRDE also revealed that n for Fe_{SAC}–NC was 3.97 and the H_2O_2 yield of Fe_{SAC}–NC was measured to be below 4%, confirming high selectivity for the 4-electron ORR. However, the yield of H_2O_2 increases significantly in the high overpotential region of FeN_4 (Fig. S12, ESI†). The electrochemical active surface area of Fe_{SAC}–NC measured by the double-layer capacitance (C_{dl}) was 30.5 mF cm^{-2}, lower than that of FeN_4 (34.4 mF cm^{-2}) (Fig. S13 and S14, ESI†). All of these verify the key role of medium spin Fe^{3+} in improving the ORR intrinsic activity.

Chronoamperometric response curves measured for Fe_{SAC}–NC and commercial Pt/C are shown in Fig. 3(e). After 80 000 seconds at a potential 0.6 V, the commercial Pt/C electrode displayed a dramatical reduction in the voltammetric current by approximately 31.8% with respect to the original value. In sharp contrast, Fe_{SAC}–NC retains up to 92.9% of its initial current under identical conditions, which manifests much-improved stability for ORR. The TEM, XRD, and Raman for

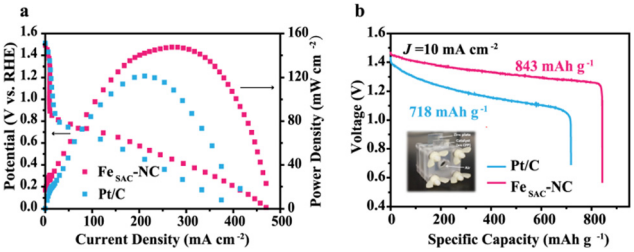

Fig. 4 (a) Discharging polarization curves and the corresponding power density plots of zinc–air battery with Fe_{SAC}–NC and Pt/C. (b) Specific capacity of zinc–air battery with Fe_{SAC}–NC and Pt/C.

80 000 seconds of electrocatalysis are provided, as shown in Fig. S15 (ESI†). No obvious changes were observed in the above characterizations for post-catalysis Fe_{SAC}–NC, which suggested that both structures and properties of the catalyst were well retained. Fig. 3(f) shows the continuous cycling for 100k cycles between 0.6 and 1.1 V. After 100k cycles, the half-wave potential of Fe_{SAC}–NC has a slight shift of 10 mV, indicating a robust ORR performance.

The tolerance to methanol crossover is important for practical applications such as direct methanol fuel cells. The methanol tolerance was evaluated by adding a 3 M methanol solution during the stability test (Fig. S16, ESI†). Fe_{SAC}–NC still maintained a high catalytic activity in the presence of methanol, demonstrating good tolerance to methanol. On the contrary, the commercial Pt/C showed a sharp jump in the current density due to the oxidation reaction of methanol.

We further assembled a zinc–air battery to demonstrate the potential of Fe_{SAC}–NC in practical applications. Fe_{SAC}–NC-based battery delivers a higher maximum power density and discharge voltage at the same current density than the Pt/C-based battery (Fig. 4(a)), confirming the high ORR activity of Fe_{SAC}–NC in the device. As shown in Fig. 4(b), the zinc–air battery with Fe_{SAC}–NC cathode shows a discharge-specific capacity of 843 mA h g^{-1} at a current density of 10 mA cm^{-2}, higher than that of Pt/C (718 mA h g^{-1}).

3.3 Activity origin for Fe–N–C with e_g^1

To understand the origin of the medium spin Fe(III) (e_g^1) activity in Fe–N–C catalysts, DFT calculations were carried out. Based on ICP, XPS, XAFS, and ^{57}Mössbauer spectroscopy analyses, Fe_{SAC}–NC involves a Fe central atom surrounded by four N atoms in the first shell, with N=C–N configuration in the second shell. Seventeen possible structures were constructed to assess their ORR activity, as shown in Fig. S17 (ESI†), and marked as Fe_{SAC}–N_XC (X = 1–17), where x stands for different configurations of the N=C–N. Both the formation energy of Fe_{SAC}–N_XC and the binding energy of the single-atom Fe sites indicate that Fe_{SAC}–N_XC is thermodynamically stable (Fig. S18, ESI†). As shown in Fig. S19 (ESI†), the electrons are transferred from Fe to N and further migrated to the N=C group, resulting in a distinct depletion of charge density on the Fe site, which is consistent with the results of XAS and XPS.

To probe the effect of the N=C–N configuration on the electronic structure of metal Fe atoms, the density of states

(DOS) of Fe_{SAC}–NC and FeN_4 near the Fermi level, mainly originating from the 3d state, were investigated. Remarkably, the $3d_{x^2-y^2}$ and $3d_{xy}$ orbitals of all Fe–N–C catalysts are either fully unoccupied or occupied, indicating that these orbitals are not engaged in bonding with oxygen-containing intermediates (Fig. S20, ESI†). The magnetic moment, however, comes from

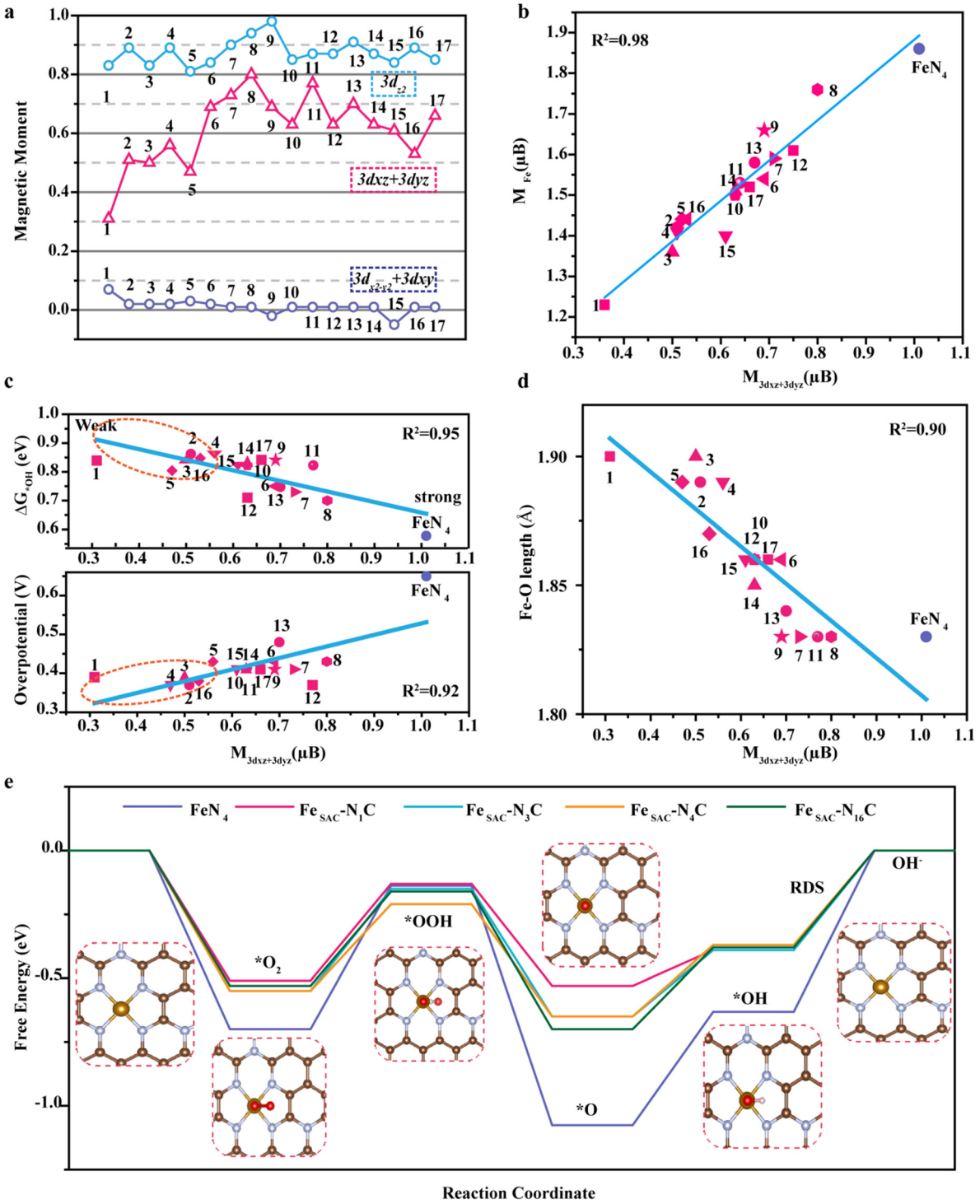

Fig. 5 (a) The magnetic moment of $3d_{z^2}$, $3d_{xz}$ + $3d_{yz}$, and $3d_{x^2-y^2}$ + $3d_{xy}$ orbital at the Fe site on Fe_{SAC}–N_xC (X = 1–17). (b) Correlation between the magnetic moment of $3d_{xz}$ + $3d_{yz}$ and magnetic moment of Fe site. (c) Correlation between the magnetic moment of $3d_{xz}$ + $3d_{yz}$, ΔG_{*OH} (up) and overpotential (down) on Fe_{SAC}–N_XC (X = 1–17). (d) Correlation between the magnetic moment of $3d_{xz}$ + $3d_{yz}$ and the Fe–O bond length on *OH@Fe_{SAC}–N_XC (X = 1–17). (e) The free energy diagrams of ORR pathways on Fe_{SAC}–N_1C, Fe_{SAC}–N_3C, Fe_{SAC}–N_5C, and Fe_{SAC}–$N_{16}C$ at U = 1.23 V *vs.* RHE. Note: 1–17 here represent Fe_{SAC}–N_1C to Fe_{SAC}–$N_{17}C$, respectively.

the spin splitting of partially occupied $3d_{z^2}$, $3d_{xz}$, and $3d_{yz}$ orbitals, implying the magnetic moments of these orbitals govern the ORR activity. The magnetic moments of $3d_{x^2-y^2}$ + $3d_{xy}$, $3d_{z^2}$, $3d_{xz}$ + $3d_{yz}$ orbitals of Fe_{SAC}–N_XC were calculated, and it is concluded that the presence of the N═C–N configurations obviously changes the magnetic moments of $3d_{xz}$ + $3d_{yz}$ orbitals and the magnetic moments of the $3d_{xz}$ + $3d_{yz}$ orbitals is nearly linear in relationship with that of the magnetic moments of metal Fe (Fig. 5(a) and (b)). Simultaneously, we also found a nearly linear relationship between the magnetic moment of $3d_{xz}$ + $3d_{yz}$ orbitals, ΔG_{*OH} (an important ORR descriptor),[41] and overpotential, revealing that the magnetic moment of $3d_{xz}$ + $3d_{yz}$ orbitals can reflect the origin of ORR activity (Fig. 5(c)). The change in the free energy of *OH@Fe_{SAC}–N_XC ranged from 0.75 to 0.87 eV, which is much larger than the *OH@Fe–N_4 site (0.58 eV). The weak adsorption of *OH on Fe_{SAC}–N_XC is the key to improving the ORR activity. Compared with FeN_4, the magnetic moment of $3d_{xz}$ + $3d_{yz}$ of Fe_{SAC}–N_XC is significantly reduced, which can weaken the interaction between *OH and Fe sites and promote the desorption of *OH. However, the theoretical overpotential of the Fe_{SAC}–N_XC ranges from 0.37 eV to 0.48 eV, revealing that the activities of the active sites with the e_g^1 electron configuration are not identical. Meanwhile, the Fe–O bond of *OH@Fe_{SAC}–N_XC decreased with the increase of $3d_{xz}$ + $3d_{yz}$ magnetic moment (Fig. 5(d)). This is due to the different hybridization modes brought about by the orbital heights of $3d_{z^2}$ and $3d_{xz}$ ($3d_{yz}$) orbitals.[42] Specifically, when the Fe–O bond length is short, $3d_{xz}$ + $3d_{yz}$ and $3d_{z^2}$ orbitals participate in the hybridization. On the contrary, the contribution of $3d_{xz}$ + $3d_{yz}$ orbital is greatly reduced when the Fe–O bond is longer (Fig. S21, ESI†).

All of these verify that the insertion of neighbouring N═C–N configurations with high electronegativity modifies the degree of hybridization between Fe $3d_{z^2}$, $3d_{xz}$, $3d_{yz}$, and oxygen-containing intermediates π* orbitals, and weakens the interaction between the oxygen-containing intermediates and Fe centers, thus improving the ORR activity. However, the seventeen possible structures show significantly different activity although they all have e_g^1, indicating that a more accurate and intrinsic indicator is needed to predict the activity. Actually, our results show a linear relationship between the intrinsic ORR activity and magnetic moment of $3d_{xz}$ + $3d_{yz}$, suggesting magnetic moment as an ideal activity descriptor. Based on the descriptor, we screened four favorable structures with high activity, namely Fe_{SAC}–N_1C, Fe_{SAC}–N_3C, Fe_{SAC}–N_4C, and Fe_{SAC}–$N_{16}C$. It should be noted that the calculated average Fe–N bond length of them is about 1.90 ± 0.01 Å, which is consistent with the experimental results of EXAFS from XAS (Fig. S21 and Table S7, ESI†). We then used the four most possible structures to fully investigate the overall ORR pathway on Fe_{SAC}–NC. Fig. 5(e) shows the Gibbs free energy variation diagram of the reaction under U = 1.23 V *vs.* RHE (Tables S8 and S9, ESI†). As seen, there is both high O_2 activation barrier (0.70 eV) and *OH desorption barrier (0.63 eV) on FeN_4, limiting the ORR activity. Contrarily, barriers for both the *OOH formation and *OH desorption are significantly decreased on Fe_{SAC}–N_XC, indicating that the spin state manipulation promotes the effective balance between O_2 activation and *OH desorption. The overpotentials of Fe_{SAC}–N_1C, Fe_{SAC}–N_3C, Fe_{SAC}–N_4C, and Fe_{SAC}–$N_{16}C$ are determined to be 0.39, 0.39, 0.37, and 0.38 V, respectively. Overall, the N═C–N configuration-induced medium spin Fe^{3+} altered Fe $3d_{z^2}$, $3d_{xz}$, $3d_{yz}$ hybridization with the oxygen-containing intermediates π* orbitals, and better-balanced O_2 activation and *OH desorption, thus improving the catalytic performance of ORR. Furthermore, the magnetic moment of $3d_{xz}$ + $3d_{yz}$ can be considered as a universal descriptor to predict the ORR activity for Fe–N–C catalysts even with e_g = 1 in their metal centers.

4. Conclusions

In summary, we developed a facile strategy for the synthesis of a single-atom Fe(III) N_4-dominated N-rich carbon environment, which shows great promise as an oxygen electrode in renewable energy conversion technologies. The formed medium spin Fe(III)–N_4 sites induced by innovative N═C–N configuration endows Fe(III) with favorable $3d_{z^2}$, $3d_{xz}$ ($3d_{yz}$) hybridization with the oxygen-containing intermediates π* orbitals, which is advantageous to balance O_2 activation and *OH desorption. Furthermore, the ORR activity of Fe–N–C catalysts is highly correlated with the magnetic moment of $3d_{xz}$ + $3d_{yz}$, and a smaller magnetic moment of $3d_{xz}$ + $3d_{yz}$ yields a higher ORR activity of the Fe–N–C even if their metal centers are all with e_g^1. The obtained Fe_{SAC}–NC exhibits extraordinary ORR catalytic performance in alkaline aqueous electrolytes, even surpassing the commercial Pt/C catalyst. In a homemade zinc–air battery, the Fe_{SAC}–NC electrode delivered a slightly higher maximum power density and discharge-specific capacity. Our finding offers new insight into the M–N–C ORR activity origin and provides a guideline to develop highly efficient noble metal-free catalysts.

Author contributions

J.-J. Z., and Z.-F. H. designed the studies. F. L. and C. S. synthesized the catalysts, performed the catalytic tests, and conducted STEM, XPS, Mössbauer spectrum, and XAFS measurements. F. L. performed the density functional theory calculations. F. L. wrote the paper with the help of L. P. and X. Z. All authors discussed the results and commented on the manuscript.

Conflicts of interest

The authors declare no conflicts of interest.

Acknowledgements

The authors appreciate the support from the National Key R&D Program of China (2020YFA0710000), the National Natural Science Foundation of China (22161142002, 22008170, and 22121004), and the Applied Basic Research Program of Qinghai Province (2023-ZJ-701). The authors acknowledge the assistance of XAS characterization and analyses from 1W1B XAFS at

Beijing Synchrotron Radiation, Institute of High Energy Physics, Chinese Academy of Sciences, Beijing, China.

References

1 R. Gao, J. Wang, Z.-F. Huang, R. Zhang, W. Wang, L. Pan, J. Zhang, W. Zhu, X. Zhang, C. Shi, J. Lim and J.-J. Zou, *Nat. Energy*, 2021, **6**, 614–623.
2 K. Li, R. Zhang, R. Gao, G.-Q. Shen, L. Pan, Y. Yao, K. Yu, X. Zhang and J.-J. Zou, *Appl. Catal., B*, 2019, **244**, 536–545.
3 M. Luo, Z. Zhao, Y. Zhang, Y. Sun, Y. Xing, F. Lv, Y. Yang, X. Zhang, S. Hwang, Y. Qin, J.-Y. Ma, F. Lin, D. Su, G. Lu and S. Guo, *Nature*, 2019, **574**, 81–85.
4 L. Chong, J. Wen, J. Kubal, F. G. Sen, J. Zou, J. Greeley, M. Chan, H. Barkholtz, W. Ding and D.-J. Liu, *Science*, 2018, **362**, 1276–1281.
5 H. T. Chung, D. A. Cullen, D. Higgins, B. T. Sneed, E. F. Holby, K. L. More and P. Zelenay, *Science*, 2017, **357**, 479–483.
6 X. Ge, A. Sumboja, D. Wuu, T. An, B. Li, F. W. T. Goh, T. S. A. Hor, Y. Zong and Z. Liu, *ACS Catal.*, 2015, **5**, 4643–4667.
7 J. Woo, J. S. Lim, T. Lim, D. S. Baek, J. H. Kim, J. H. Lee, H. Y. Jeong, C. H. Choi and S. H. Joo, *EES. Catal.*, 2023, **1**, 62–73.
8 N. Zhang, T. Zhou, M. Chen, H. Feng, R. Yuan, C. A. Zhong, W. Yan, Y. Tian, X. Wu, W. Chu, C. Wu and Y. Xie, *Energy Environ. Sci.*, 2020, **13**, 111–118.
9 C. Tang, L. Chen, H. Li, L. Li, Y. Jiao, Y. Zheng, H. Xu, K. Davey and S. Z. Qiao, *J. Am. Chem. Soc.*, 2021, **143**, 7819–7827.
10 X. Wan, X. Liu, Y. Li, R. Yu, L. Zheng, W. Yan, H. Wang, M. Xu and J. Shui, *Nat. Catal.*, 2019, **2**, 259–268.
11 M. Zhu, C. Zhao, X. Liu, X. Wang, F. Zhou, J. Wang, Y. Hu, Y. Zhao, T. Yao, L.-M. Yang and Y. Wu, *ACS Catal.*, 2021, **11**, 3923–3929.
12 Y. Wang, Y.-J. Tang and K. Zhou, *J. Am. Chem. Soc.*, 2019, **141**, 14115–14119.
13 X. T. Wang, T. Ouyang, L. Wang, J. H. Zhong, T. Ma and Z. Q. Liu, *Angew. Chem., Int. Ed.*, 2019, **58**, 13291–13296.
14 W. Zhong, Y. Qiu, H. Shen, X. Wang, J. Yuan, C. Jia, S. Bi and J. Jiang, *J. Am. Chem. Soc.*, 2021, **143**, 4405–4413.
15 W. Cheng, P. Yuan, Z. Lv, Y. Guo, Y. Qiao, X. Xue, X. Liu, W. Bai, K. Wang, Q. Xu and J. Zhang, *Appl. Catal., B*, 2020, **260**, 118198.
16 Z. Chen, H. Niu, J. Ding, H. Liu, P.-H. Chen, Y.-H. Lu, Y.-R. Lu, W. Zuo, L. Han, Y. Guo, S.-F. Hung and Y. Zhai, *Angew. Chem., Int. Ed.*, 2021, **60**, 25404–25410.
17 J. Yan, Y. Wang, Y. Zhang, S. Xia, J. Yu and B. Ding, *Adv. Mater.*, 2021, **33**, e2007525.
18 G. Yang, J. Zhu, P. Yuan, Y. Hu, G. Qu, B.-A. Lu, X. Xue, H. Yin, W. Cheng, J. Cheng, W. Xu, J. Li, J. Hu, S. Mu and J.-N. Zhang, *Nat. Commun.*, 2021, **12**, 1734.
19 J. Suntivich, K. J. May, H. A. Gasteiger, J. B. Goodenough and Y. Shao-Horn, *Science*, 2011, **334**, 1383–1385.
20 W. Liu, L. Zhang, X. Liu, X. Liu, X. Yang, S. Miao, W. Wang, A. Wang and T. Zhang, *J. Am. Chem. Soc.*, 2017, **139**, 10790–10798.
21 R. Nityananda, *J. Sci. Educ.*, 2017, **22**, 809.
22 X. Li, X. Yang, L. Liu, H. Zhao, Y. Li, H. Zhu, Y. Chen, S. Guo, Y. Liu, Q. Tan and G. Wu, *ACS Catal.*, 2021, **11**, 7450–7459.
23 M. Xiao, Z. Xing, Z. Jin, C. Liu, J. Ge, J. Zhu, Y. Wang, X. Zhao and Z. Chen, *Adv. Mater.*, 2020, **32**, 2004900.
24 J. Zhao, J. Chen, S. Xu, M. Shao, Q. Zhang, F. Wei, J. Ma, M. Wei, D. G. Evans and X. Duan, *Adv. Funct. Mater.*, 2014, **24**, 2938–2946.
25 H. Zhang, W. Cheng, D. Luan and X. W. Lou, *Angew. Chem., Int. Ed.*, 2021, **60**, 13177–13196.
26 Y. Zheng, Y. Jiao, Y. Zhu, L. H. Li, Y. Han, Y. Chen, A. Du, M. Jaroniec and S. Z. Qiao, *Nat. Commun.*, 2014, **5**, 3783.
27 S. M. Kirtley, O. C. Mullins, J. Chen, J. Vanelp, S. J. George, C. T. Chen, T. Ohalloran and S. P. Cramer, *Biochim. Biophys. Acta*, 1992, **1132**, 249–254.
28 K. Fujii, K. Akamatsu and A. Yokoya, *J. Phys. Chem. B*, 2004, **108**, 8031–8035.
29 Y. Luo, Y. Chen, Y. Xue, J. Chen, G. Wang, R. Wang, M. Yu and J. Zhang, *Small*, 2022, **18**, 2105594.
30 L. Lin, Z. K. Yang, Y.-F. Jiang and A.-W. Xu, *ACS Catal.*, 2016, **6**, 4449–4454.
31 J. Wan, Z. Zhao, H. Shang, B. Peng, W. Chen, J. Pei, L. Zheng, J. Dong, R. Cao, R. Sarangi, Z. Jiang, D. Zhou, Z. Zhuang, J. Zhang, D. Wang and Y. Li, *J. Am. Chem. Soc.*, 2020, **142**, 8431–8439.
32 J. Qin, H. Liu, P. Zou, R. Zhang, C. Wang and H. L. Xin, *J. Am. Chem. Soc.*, 2022, **144**, 2197–2207.
33 J. Feng, H. Gao, L. Zheng, Z. Chen, S. Zeng, C. Jiang, H. Dong, L. Liu, S. Zhang and X. Zhang, *Nat. Commun.*, 2020, **11**, 4341.
34 U. I. Koslowski, I. Abs-Wurmbach, S. Fiechter and P. Bogdanoff, *J. Phys. Chem. C*, 2011, **115**, 23417–23427.
35 U. I. Koslowski, I. Abs-Wurmbach, S. Fiechter and P. Bogdanoff, *J. Phys. Chem. C*, 2008, **112**, 15356–15366.
36 U. I. Kramm, M. Lefevre, N. Larouche, D. Schmeisser and J. P. Dodelet, *J. Am. Chem. Soc.*, 2014, **136**, 978–985.
37 A. Zitolo, V. Goellner, V. Armel, M. T. Sougrati, T. Mineva, L. Stievano, E. Fonda and F. Jaouen, *Nat. Mater.*, 2015, **14**, 937–942.
38 Y. Liu, X. Liu, Z. Lv, R. Liu, L. Li, J. Wang, W. Yang, X. Jiang, X. Feng and B. Wang, *Angew. Chem., Int. Ed.*, 2022, **61**, e202117617.
39 Q. Cheng, L. Yang, L. Zou, Z. Zou, C. Chen, Z. Hu and H. Yang, *ACS Catal.*, 2017, **7**, 6864–6871.
40 E. Luo, H. Zhang, X. Wang, L. Gao, L. Gong, T. Zhao, Z. Jin, J. Ge, Z. Jiang, C. Liu and W. Xing, *Angew. Chem., Int. Ed.*, 2019, **58**, 12469–12475.
41 H.-x Zhong, J. Wang, Y.-w Zhang, W.-l Xu, W. Xing, D. Xu, Y.-f Zhang and X.-b Zhang, *Angew. Chem., Int. Ed.*, 2014, **53**, 14235–14239.
42 Z. Fu, B. Yang and R. Wu, *Phys. Rev. Lett.*, 2020, **125**, 156001.